Exceptional Electron Conduction in Two-Dimensional Covalent Organic Frameworks

Enquan Jin,[1,8] Keyu Geng,[1,8] Shuai Fu,[2] Sheng Yang,[3] Narissa Kanlayakan,[4,6] Matthew A. Addicoat,[5] Nawee Kungwan,[6] Johannes Geurs,[3] Hong Xu,[1] Mischa Bonn,[2] Hai I. Wang,[2] Jurgen Smet,[3] Tim Kowalczyk,[4] and Donglin Jiang[1,7,9,]*

[1]Department of Chemistry, Faculty of Science, National University of Singapore, 3 Science Drive 3, Singapore 117543, Singapore

[2]Max Planck Institute for Polymer Research, Ackermannweg 10, D-55128 Mainz, Germany

[3]Max Planck Institute for Solid State Research, Heisenbergstraße 1, 70569 Stuttgart, Germany

[4]Department of Chemistry, Advanced Materials Science and Engineering Centre and Institute for Energy Studies, Western Washington University, Bellingham, WA 98225, USA

[5]School of Science and Technology, Nottingham Trent University, Clifton Lane, Nottingham, NG11 8NS, United Kingdom

[6]Department of Chemistry and Centre of Excellence in Materials Science and Technology, Chiang Mai University, Chiang Mai 50200, Thailand

[7]Joint School of National University of Singapore and Tianjin University, International Campus of Tianjin University, Binhai New City, Fuzhou 350207, China

[8]Equal Contribution.

[9]Lead Contact.

*Correspondence: chmjd@nus.edu.sg

SUMMARY

Most organic/polymeric semiconductors are *p*-type semiconductors while their *n*-type versions are limited in both availability and carrier mobility. How to develop high-rate *n*-type organic/polymeric semiconductors remains challenging. Here we report an approach to high-rate *n*-type semiconductors *via* topology-directed polycondensation of conventional *p*-type knots with *n*-type isoindigo linkers to form non-conjugated tetragonal and hexagonal two-dimensional polymeric frameworks. The polymers are planar in conformation and show flattened frontier levels which enable electron to move along the non-conjugated polymeric backbones. The eclipsed face-to-face stack reduces reorganization energy and greatly strengthens electronic coupling, thus enabling band-like electron conduction perpendicular to polymer layers. A device record electron mobility as high as 8.2 cm^2 V^{-1} s^{-1} is achieved with Hall effect measurements, while time- and frequency-resolved terahertz spectroscopy revealed a benchmark mobility of 13.3 cm^2 V^{-1} s^{-1}. These new mechanistic insights with exceptional mobility open a way to high-rate *n*-type organic/polymeric semiconductors.

Covalent organic frameworks, organic semiconductor, electron mobility, charge carrier transport, band-link conduction, Hall effect measurement, Time- and frequency-resolved terahertz spectroscopy, computation

INTRODUCTION

Semiconductors are key elements in solar cells, light-emitting diodes, and thermoelectric generators where electron transport is the basic process which governs their performance.[1,2] Traditionally, non-conjugated organic/polymeric materials like saturated polyhydrocarbons and plastics are insulators because their valence bands are fully occupied with electrons while these electrons are locked by atoms and cannot move to conduction bands. In order to allow charge motion in organic/polymeric materials, introduction of π conjugation to materials backbone has been the sole way. This paradigm has developed organic/polymeric semiconductors as observed in oligomers or one-dimensional (1D) π-conjugated polymers.[3,4] In order to allow electron motion, the π-conjugated backbone must be electron deficient and possesses a low enough conduction band.[5,6] In organic/polymeric materials, as conduction band consists of more lobes than valence band, electron is inherently far more difficult to move than hole and generally electron has a low mobility by orders of magnitude compared to its counterpart – hole. Moreover, at macroscopic level, electron motion is further difficult as electrons are easily to get trapped by structural defects and to dissipate by impurities.[7–9] As a result, most organic semiconductors are *p*-type for hole transport other than *n*-type for electron conduction.

The Bigger Picture

In contrast to inorganic semiconductors, organic/polymeric semiconductors usually have limited mobility owing to their structural nature. Especially, enabling electron conduction with high carrier mobility is extremely difficult.

Herein, we solve this problem by organizing electron-deficient isoindigo unit to form well-ordered yet non-conjugated covalent organic frameworks, constituting two-dimensional polygonal backbones and ordered columnar π arrays via face-to-face stack. Hall effect measurements, time- and frequency-resolved terahertz spectroscopy as well as theoretical calculations mutually corroborate exceptional high-rate electron transport via band-like conduction across layers and over the non-conjugated 2D planes in the undoped frameworks. This work thus offers a new regime in high performance organic/polymeric semiconductors.

In order to enable high-rate electron transport, electron deficient π-conjugated oligomers and polymers must be organized into order structures. In real materials, most π-conjugated polymers are amorphous and lack ordered structures, while certain π oligomers or small π compounds can form crystals whose lattices are however not optimizable for electron conduction.[10,11] This dilemma leaves organic/polymeric systems under strain as there is no general strategy for designing high-rate *n*-type materials based on these traditional systems.

By looking back at the crystalline structures of π-conjugated oligomers and 1D chain conformation of π-conjugated polymers, we realized the importance of designing polymer conformation. The confirmation affects the band formation at microscopic level as well as structural ordering at macroscopic scale, thereby having a direct impact on electron conduction. In this work, we prove this concept through the combination of experimental and computational approaches to design electron-deficient two-dimensional (2D) polymers with well-defined planar conformation and face-to-face stacking, so that the molecular orderings are established in a three-dimensional way to constitute periodic 2D polygonal backbones over the *x-y* plane and extended layer frameworks along the *z* direction perpendicular to the 2D plane. We disclose their structural features and unique electron conduction mechanisms by highlighting their exceptional intrinsic electron mobility.

Covalent organic frameworks (COFs) are a class of crystalline polymer which integrate π units into 2D polymers, which further stack to yield periodically ordered columnar π arrays.[12-17] The specific topological diagram renders the construction of built-in π columns that can serve as preorganized pathways for carrier transport. Those distinct structures and functions of COFs are hardly accessible by other self-assemblies, polymers or even single crystals. Thus, COFs offer a novel and unreplaceable platform for designing semiconductors.[18-20] By virtue of such unique structures, several 2D COFs have been developed *via* polycondensation of predesigned knot and linker units that enable to produce ordered lateral structure over the *x-y* plane as well as well-defined π stack along the *z* direction.[12, 21-26] Among them, most reported 2D COFs are *p*-type semiconductors.[21-24] Although these structural features are attractive for construction of n-type semiconductors, however, *n*-type COFs are still very limited in structure diversity and carrier mobility while their conducting mechanisms remain unclear.[25, 26]

In this study, we showed electron conduction mechanisms and demonstrated ultrahigh electron mobility in non-conjugated electron-deficient isoindigo COFs, which possess a completely planar conformation in which π clouds of building units can be unidirectionally aligned on the top and bottom of the *x-y* plane to ensure lateral overlap among frontier orbitals. The 2D COFs with 2D electron-deficient sheets stacked in a discrete eclipsed manner develop π arrays to offer vertical pathway. The completely planar structure and face-to-face stack not only greatly reduce reorganization energy of carrier transport but also trigger electronic couplings as revealed by computational calculations. Remarkably, these effects lead to two findings of this unprecedented class of *n*-type organic/polymeric semiconductors, i.e. high electron transport in the non-conjugated polymer backbones and band-like electron conduction across the layers. These new mechanisms and exceptional mobility open a new phase for designing high-rate electron-transporting organic/polymeric semiconductors.

RESULTS AND DISCUSSION

DESIGN PRINCIPLE

We designed two non-conjugated yet 2D isoindigo polymers and their layer frameworks with hexagonal and tetragonal topologies to demonstrate our new paradigm (Figure 1A and B). In HHTP-MIDA-COF (Figure 1C) and CuPc-MIDA-COF (Figure 1D), all the segments of the knot, linker and boronate ester linkage are rigid and planar, so that the 2D polymer sheets adopt a flat conformation and are shape-persistent. Notably, each hexagonal and tetragonal backbone consists of 12 and 8 non-conjugated boronate linkages, respectively. They constitute non-conjugated yet extended 2D polymers (Figure 1C and d and Inset). The face-to-face stacked 2D sheets form layered HHTP-MIDA-COF (Figure 1E) and CuPc-MIDA-COF (Figure 1F) to create ordered π arrays. Unexpectedly we found that the 2D frameworks exhibit ultrahigh electron transport in the non-conjugated polymer backbones and band-like conduction across the layers.
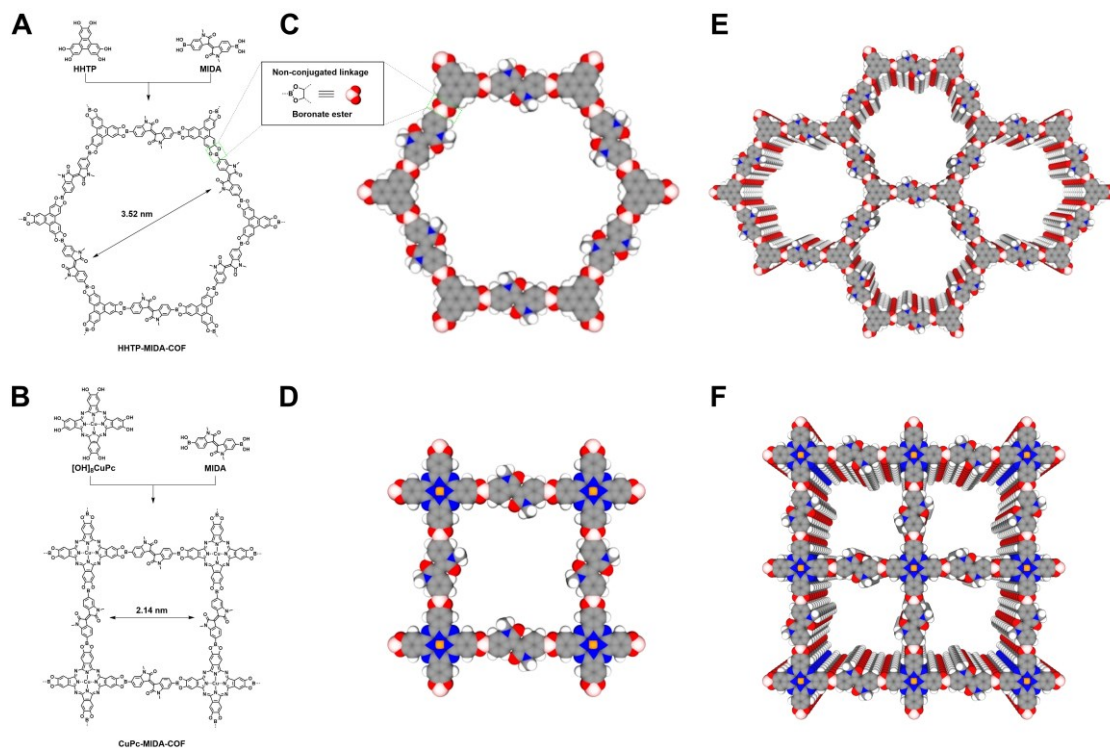
Figure 1. Structures of Electron-Conducting Non-Conjugated Two-Dimensional Polymers

(A and B) Schematics of non-conjugated 2D polymers of (A) hexagonal HHTP-MIDA-COF with triphenylene knot and isoindigo linker and (B) tetragonal CuPc-MIDA-COF with phthalocyanine knot and isoindigo linker via boronate ester linkages.

(C and D) Reconstructed 2D polymer structures of (C) one hexagonal backbone and (D) one tetragonal backbone of CuPc-MIDA-COF. The 2D polymer backbones are planar and extend over the x-y plane. Inset: Non-conjugated boronate ester linkage between knot and linker units; there are 12 and 8 non-conjugated linkages in each hexagon and tetragon macrocycle, respectively.

(E and F) Reconstructed face-to-face stack structures of 10 layers of (E) HHTP-MIDA-COF and (F) CuPc-MIDA-COF (four pores are shown). Grey, C; white, H; red, O; blue, N; pink, B; orange: Cu.

A strong electron-deficient unit like isoindigo is necessary to form the lowest unoccupied molecular orbital (LUMO) or conduction band that enables electron conduction. Isoindigo is one of the natural pigments and has been used as a strong electron acceptor for the synthesis of conjugated polymers.[27-30] With strong electron affinity and narrow bandgap, isoindigo-based conjugated polymers possess shallow HOMO and deep LUMO energy levels, which is desired for electron conduction. Meanwhile, isoindigo motif possesses an exceptional dipole moment originated from the carbonyl functionality, which enables strong intermolecular interactions. However, isoindigo-based semiconductors usually have limited intermolecular charge carrier conduction owing to their less effective π stacking.[27, 28] We utilized isoindigo to explore electron-deficient COFs via topology-directed polymerization to confine the isoindigo into well-defined 2D polymer structures and highly ordered face-to-face stack, enabling to revealing its unusual capability of constructing of *n*-type organic/polymeric semiconductors. 2D non-conjugated COFs with isoindigo units are unprecedented.
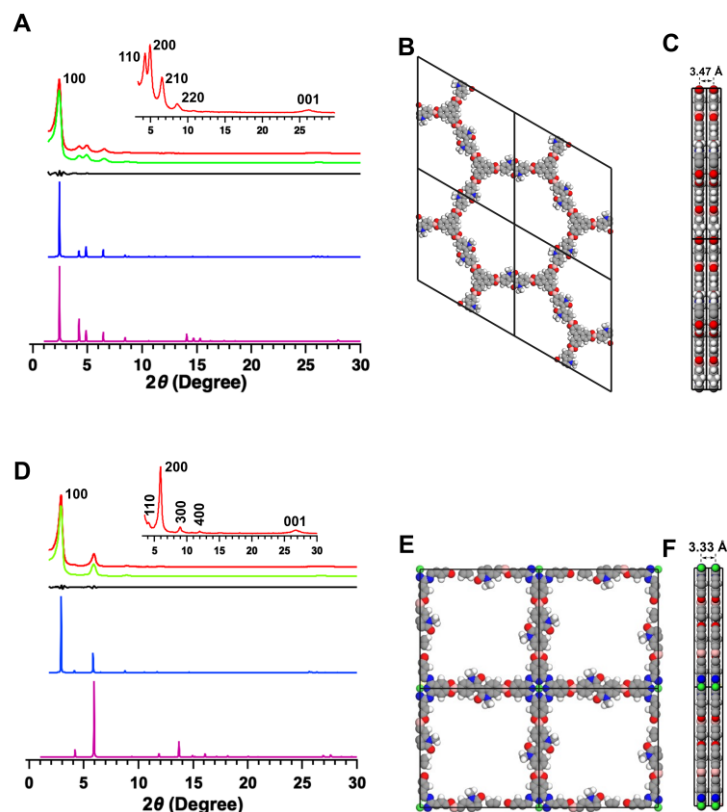
Figure 2. Crystal Structures

(A) PXRD patterns of HHTP-MIDA-COF and simulations. From top to bottom: experimentally observed pattern (red), Pawley-refined pattern (green), the difference between both patterns (black), the modes for AA-stacking (blue) and AB-stacking (purple). The number corresponds to the facet of each peak.

(B) Reconstructed unit cell of HHTP-MIDA-COF.

(C) Reconstructed layered structure of HHTP-MIDA-COF.

(D) PXRD patterns of CuPc-MIDA-COF and simulations. From top to bottom: experimentally observed pattern (red), Pawley-refined pattern (green) difference between both patterns (black), the modes for AA-stacking (blue) and AB-stacking (purple). The numbers correspond to the facet of each peak.

(E) Reconstructed unit cell of CuPc-MIDA-COF.

(F) Reconstructed layered structure of CuPc-MIDA-COF. Grey, C; white, H; red, O; blue, N; pink, B; green: Cu.

SYNTHESIS

We synthesized HHTP-MIDA-COF and CuPc-MIDA-COF via topology-guided polymerization (Figure 1A and B).[12, 18, 31-32] The reaction exploits the condensation of C_2-symmetric 6, 6'-N,N'-(2-methyl)-isoindigo diboronic acid (MIDA) as linker with C_3-symmetric 2, 3, 6, 7, 10, 11-hexahydroxytriphenylene (HHTP) or C_4-symmetric copper(II) 2, 3, 9, 10, 16, 17, 23, 24-octakishydroxyphthalocyanine ([OH]$_8$CuPc) as knot, to produce 2D hexagonal and tetragonal frameworks with a yield of 89% and 91%, respectively (see Experimental procedures).

STRUCTURAL CHARACTERIZATIONS

We characterized the chemical structures of HHTP-MIDA-COF and CuPc-MIDA-COF with various analytical methods (see Experimental procedures, Figures S1-S11 and Tables S1-S9). Fourier-transform infrared spectroscopy revealed the formation of HHTP-MIDA-COF and CuPc-MIDA-COF via boronate ester linkages through vibration bands at 956, 1168, 1245, and 1343 cm^{-1}. These were assigned to the C–B, C–O, C–B, and B–O stretches,[18] respectively (Figure S5). Elemental analysis showed that the C, H and N contents were close to their theoretical values (see Experimental procedures). A thermogravimetric analysis confirmed that HHTP-MIDA-COF and CuPc-MIDA-COF are stable up to 400 °C under nitrogen (Figure S6).

The Powder X-ray diffraction (PXRD) peaks of HHTP-MIDA-COF at 2.42°, 4.22°, 4.92°, 6.50°, 8.56°, and 26.24° can be assigned to the (100), (110), (200), (210), (220), and (001) facets, respectively (Figure 2A, red curve). The Pawley refined PXRD pattern (Figure 2A, green curve; for atomistic coordinates, see Table S1) using the $P6/m$ space group with cell parameters of a = b = 41.3449 Å, c = 3.5309 Å, $\alpha = \beta$ = 90°, and γ = 120° reproduced the observed curve without any significant deviations (Figure 2A, black curve). We optimized the stacking structure using the density-functional tight-binding (DFTB+) method including Lennard-Jones (LJ) dispersion.[33, 34] The AA-stacking mode (Figure 2B; for atomistic coordinates, see Table S2) generated a PXRD pattern (Figure 2A, blue curve) that agrees with the observed profile. Therefore, the structure reconstruction revealed a shape-persistent and extended 2D hexagonal lattice (hcb net) (Figure 2B). The presence of the (001) facet at 26.24° suggests the structural ordering along the z-direction with an interlayer separation of 3.47 Å (Figure 2C).

The CuPc-MIDA-COF exhibited diffraction peaks at 2.94°, 4.16°, 5.89°, 8.85°, 11.80°, and 26.78°, which were assigned to the (100), (110), (200), (300), (400), and (001) facets, respectively (Figure 2D, red curve). The Pawley refined PXRD pattern (Figure 2D, green curve; for atomistic coordinates, see Table S3) using the $P4/m$ space group with cell parameters of a = b = 29.953 Å, c = 3.5575 Å, and $\alpha = \beta = \gamma$ = 90° reproduced the experimentally observed profile as evidenced from their good agreement (Figure 2D, black curve). The CuPc-MIDA-COF assumes an AA-stacking mode (for atomistic coordinates, see Table S4), which yields a PXRD pattern (Figure 2D, blue curve) consistent with the observed one. Therefore, CuPc-MIDA-COF is a rigid 2D tetragonal polymer with the sql net (Figure 2E). The existence of the (001) facet at 26.78° indicates that the structural ordering is extended to the third z-direction perpendicular to the 2D layers at an interval of 3.33 Å (Figure 2F).

Reversible nitrogen sorption isotherms were observed for HHTP-MIDA-COF (Figure S7A) and CuPc-MIDA-COF (Figure S8A) from which Brunauer-Emmett-Teller surface areas were extracted. They were equal to 1170 and 442 $m^2 \, g^{-1}$, respectively. The HHTP-MIDA-COF (Figure S7B) and CuPc-MIDA-COF (Figure S8B) have a pore size of 3.5 and 2.1 nm, respectively. These values are consistent with their lattices.

HALL EFFECT MEASUREMENTS

We investigated the electrical conduction behavior with the Van der Pauw method.[35] The CuPc-MIDA-COF and HHTP-MIDA-COF samples were fabricated in a glove box with an argon atmosphere by exerting a pressure of 1.3 GPa (equivalent to 140.7 kg mm^{-2}) in order to shape them into thin discs with a diameter of 7 mm and a thickness of about 0.4 mm. Each pellet was mounted on a chip carrier (schematic geometry and example shown in Figures S9 and S10), contacted with indium wires and loaded into a Physical Property Measurement System (PPMS Dynacool, Quantum Design). Contrary to expectation, these COFs conduct at room temperature and it is indeed possible to characterize the material by performing magneto-transport measurements. The conductance is measured by driving a current along one side of the pellet and monitoring the voltage on the other side. The temperature dependence of the conductivity, obtained by normalizing the conductance to the sample thickness, is illustrated for CuPc-MIDA-COF in Figure 3A and for HHTP-MIDA-COF in Figure 3B. The data were also plotted on a logarithmic ordinate and inverse temperature abscissa in Figure 3C and 3D. In both cases, conduction near room temperature is thermally activated, with an activation energy of 340 meV for CuPc-MIDA-COF and 300 meV for HHTP-MIDA-COF. Noticeably, these non-doped COFs exhibited a conductivity of 10^{-6} S cm^{-1}, which is the same level as those of undoped π-conjugated polymers.[6, 8, 36]
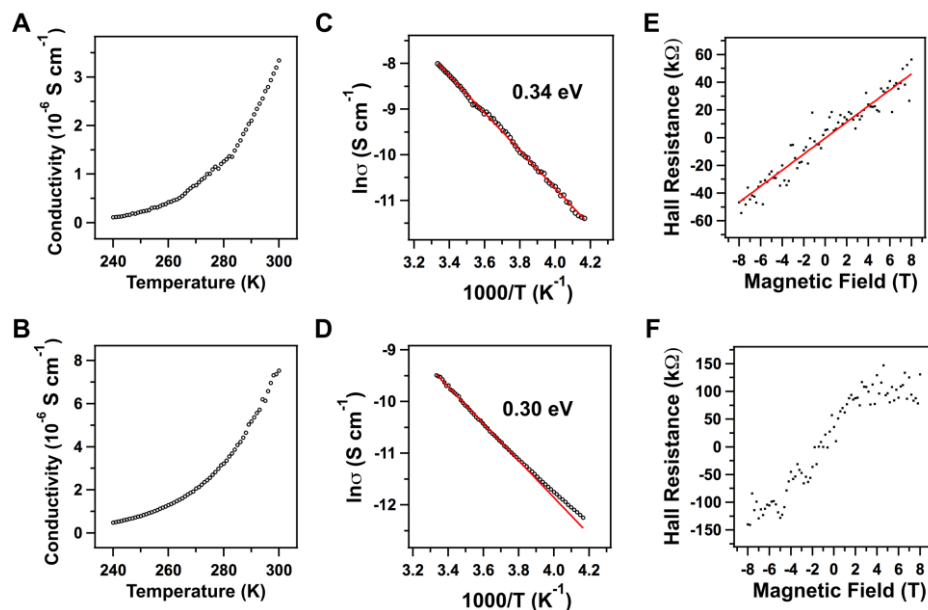
Figure 3. Conductivity and Hall Effect Measurements

(A) Electrical conductivity of CuPc-MIDA-COF as a function of temperature.

(B) Electrical conductivity of HHTP-MIDA-COF as a function of temperature.

(C and D) Plots of the natural logarithm of the conductivity (lnσ) versus inverse temperature (1000/T) of (C) CuPc-MIDA-COF and (D) HHTP-MIDA-COF.

(E) Hall effect measurement on CuPc-MIDA-COF at 300 K. The red line is a linear fit to the data.

(F) Hall effect measurement on HHTP-MIDA-COF at 300 K.

The Hall effect was exploited to identify the carrier type and quantify the carrier density. The Hall resistance of CuPc-MIDA-COF at 300 K, plotted in Figure 3E, behaves linearly across the scanned perpendicular magnetic field range from −8 T to 8 T. From the sign and slope, we conclude that the charge carriers are electrons[37] and have a density of 2.6×10^{12} cm^{-3}. With this density an estimate of the electron mobility can be obtained from the zero-field conductivity. It yields recorded electron mobility of 8.3 cm^2 V^{-1} s^{-1} for CuPc-MIDA-COF (Table S5).

The Hall resistance of HHTP-MIDA-COF, shown in Figure 3F, is non-linear instead. The curve flattens out as one moves towards fields with higher magnitude. This behavior is characteristic of materials where multiple charge carrier channels contribute to current flow. While it is not possible to separate the properties of multiple charge carriers, some conclusions can be drawn by considering a two-band model description (see Experimental procedures) to the overall shape of the Hall resistance trace. In the high field limit, the Hall resistance slope is proportional to the inverse of the total density and this yields a value of 4.5×10^{11} cm^{-3}. From the steeper slope around zero field, it can be concluded that both carrier species are electrons and that they have different densities and/or mobilities (for details see Experimental procedures). Unfortunately, it is difficult to reliably extract the mobilities and the densities of the two-carrier species of HHTP-MIDA-COF as no additional information to constrain the large parameter space is available.

TIME- AND FREQUENCY-RESOLVED TETRAHERTZ SPECTROSCOPY

To further elucidate the microscopic transport properties of charge carriers, ultrafast terahertz spectroscopy was employed to probe both the time- and frequency-resolved photoconductivity response (see Experimental procedures).[38] Figure 4A shows the real part of the photoconductivity response for CuPc-MIDA-COF following a femtosecond pulse laser excitation at 400 nm. The initially free, optically created charges exhibited a finite conductivity with a decay lifetime of 1.5 ps. This fast decay is attributed to trapping or the formation of charge-neutral bounded exciton states, which do not contribute to electrical conduction.[39]

We further quantified the frequency-resolved terahertz conductivities close to the peak of the photoconductivity dynamics where charge carriers appear free. As shown in Figure 4B, the data can be described well by the Drude-Smith model (see Experimental procedures),[39] which assumes Drude-type transport of free charges impeded by spatial confinement, e.g., by the grain boundaries. The model reveals a charge scattering time of 23 ± 13 fs for CuPc-MIDA-COF (Figure 4B) and 16 ± 12 fs for HHTP- MIDA-COF (Figure 4C and D). Employing the effective mass M* (see Experimental procedures, Table S6) from the density functional theory (DFT) calculations,[40] the intrinsic carrier mobility is estimated to be 13.3 ± 7.5 cm^2 V^{-1} s^{-1} and 3.4 ± 2.5 cm^2 V^{-1} s^{-1} for CuPc-MIDA-COF and HHTP-MIDA-COF, respectively (see Experimental procedures, Table S5). These values reveal the intrinsically high carrier mobilities. The extracted mobility for CuPc-MIDA-COF is also in line with the estimate of the electron mobility from the DC magneto-transport measurements.
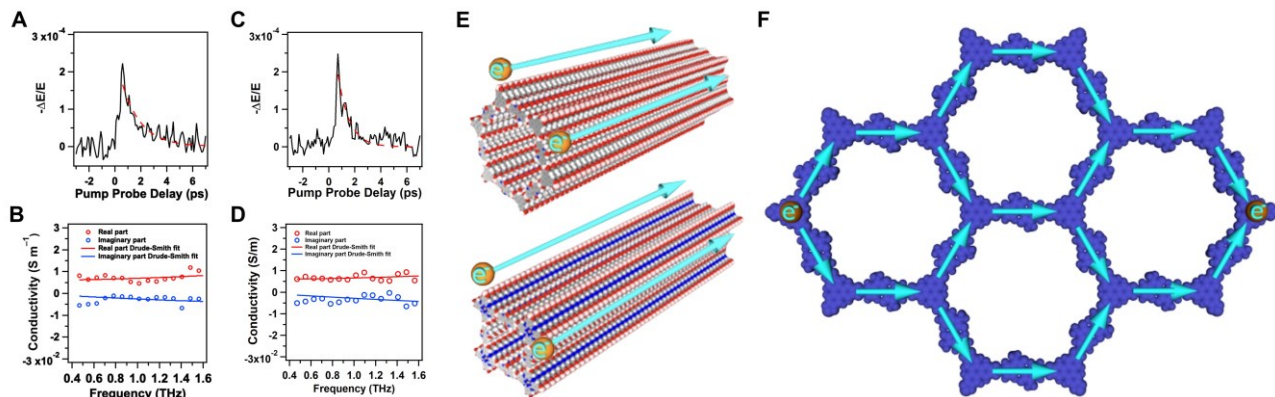

Figure 4. Time- and Frequency-Resolved Terahertz Photoconductivity and Electron Conduction Pathways

(A and B) Room-temperature time-resolved (A) and frequency-resolved (B) terahertz photoconductivity of CuPc-MIDA-COF (excitation at 400 nm with a fluence of 252 μJ cm^{-2}). The red dash line in (A) is a fit to the data with an exponential decay function. The red circles in (B) correspond to the real part of the photoconductivity, while the blue circles are the imaginary part. The solid lines in (B) are fits to the data points based on the Drude-Smith model.
(C and D) Time-resolved (C) and frequency-resolved terahertz photoconductivity (D) of HHTP-MIDA-COF (excitation at 400 nm with a fluence of 252 μJ cm^{-2}), measured at 0.5 ps after the main peak in the photoconductivity shown in (C). Red and blue points correspond to their real and imaginary parts of the photoconductivity, respectively. The solid lines are the Drude-Smith fits.
(E) Electron conduction pathways in HHTP-MIDA-COF (top panel) and CuPc-MIDA-COF (bottom panel) to cross the layers (only one pore and 50 layers are shown). Two arrows are shown to present band conduction across the layers.
(F) Electron conduction along the non-conjugated 2D hexagonal backbone in HHTP-MIDA-COF.

COMPUTATIONAL APPROACHES

It seems remarkable that the charge carrier response reflects band-like conduction. A conventional Marcus-like expression[41, 42] for incoherent carrier hopping along the z-direction across the layers was used to describe the charge transport rate and reorganization energy. Computations with constrained density functional theory configuration interaction (CDFT-CI)[43] revealed that the electronic couplings for electron transport in both COFs are larger than those for hole transport ($V_e > V_h$), which is consistent with the results of observed electron transport in the Hall effect measurements (Table S7). Analysis at the ωB97X-D/6-31G(d) level in Q-Chem 5.0 revealed a low reorganization energy of only 0.07 eV for electron transport in CuPc-MIDA-COF, while that in HHTP-MIDA-COF is 0.30 eV (Table S8).[44] The near-zero reorganization energy of CuPc-MIDA-COF suggests that the close face-to-face stacking structure of planar layers can minimize the structural reorganization energy. Nonetheless, the incoherent hopping mode yields one order of magnitude lower mobilities (Table S9) compared to those observed experimentally, suggesting that this is not the dominant transport mechanism. Presumably, the strong interlayer electron coupling in the non-

conjugated HHTP-MIDA-COF (Figure 4E, top panel) and CuPc-MIDA-COF (Figure 4E, bottom panel), enables vertical electron transport via band-like conduction to cross the z-direction stacked layers. Band-like hole transport has indeed been theoretically predicted in COFs.[45]

In the calculations we also artificially disabled the in-plane electronic connectivity of HHTP-MIDA-COF to look at contributions from the knot and linker separately. The equivalent electron mass of the knot is 5.19 M_0, while the equivalent electron mass at the linker is 3.21 M_0 (Table S6). The electron mass difference with and without in-plane coupling (Table S6) indicates that HHTP-MIDA-COF enables both in-plane (Figure 4F) and out-of-plane conduction (Figure 4E, top lane). Moreover, we calculated the lowest conduction band and observed that the band covers the whole 2D skeleton, i.e., atoms from the entire 2D layer (Figure S11) contribute to the band. It is this band feature that offers the basis for in-plane 2D electron transport along a non-conjugated polymer backbone. The electron transport along the 2D polygonal backbone would develop an atomically thick unimolecular circuit (Figure 4F). Whether the 2D electron transport over the polymer sheet is coherent requires further investigation.

CONCLUSION

In summary, we demonstrated the topology-guided growth of 2D planar polymers and in-situ formation of face-to-face stacking structures of frameworks by integrating strong electron deficient isoindigo segments, which open a door to design a novel class of high-rate *n*-type semiconductors. This approach features the advantage of a total control over both micro and macroscopic structures including components, topology, conduction pathway, and lattice via one-pot polymerization. By using cutting-edge instrumentations including Hall effect measurements and time- and frequency-resolved terahertz spectroscopy, we disclosed unique electron conduction behaviors and mechanisms. The lateral electron transport over the 2D plane and band-like electron conduction across the layers are two findings of this unprecedented class of *n*-type semiconducting framework materials.

A number of promising directions for future work can be pursued to develop high-rate electron-conducting organic materials. In addition to the present hexagonal and tetragonal skeletons, 2D polymers and COFs with trigonal, rhombic and kagome topologies are interesting for electron transport. Owing to a broad scope of electron deficient building units, we envision that the present strategy would greatly enhance the diversity of *n*-type organic/polymeric semiconductors with predesignable architectures and high-rate electron transport properties. These materials form a new platform for advanced energy storage and conversions.

EXPERIMENTAL PROCEDURES

Synthesis of 2D COFs

HHTP-MIDA-COF. A Pyrex tube (10 mL) was charged with HHTP (10.0 mg, 0.031 mmol), MIDA (17.5 mg, 0.046 mmol) and 1,4-dioxane/mesitylene (1 mL, 6/1 vol./vol.). The mixture was sonicated for 30 seconds, degassed through three freeze–pump–thaw cycles, sealed under vacuum and heated at 90 °C for 3 days. The reaction mixture was cooled at room temperature and the dark red precipitate was collected by centrifugation. The precipitate was washed with anhydrous THF (100 mL × 3) and anhydrous acetone (100 mL × 3), centrifuged and dried under vacuum at room temperature for 24 h, to obtain HHTP-MIDA-COF as a dark red powder with an 89% yield. Elemental analysis: Calcd. C (69.02%), H (3.07%), N (5.37%). Found C (64.88%), H (4.63%), N (6.87%).

CuPc-MIDA-COF. To a Pyrex tube (10 mL), $[OH]_8$CuPc (10.0 mg, 0.014 mmol), MIDA (10.8 mg, 0.028 mmol) and DMAc/*o*-DCB (1 mL, 2/1 vol./vol.) was added. The mixture was sonicated for 30 seconds, degassed through three freeze–pump–thaw cycles, sealed under vacuum and heated at 120 °C for 3 days. The reaction mixture was cooled down to room temperature and the dark red precipitate was collected by centrifugation. The precipitate was washed with anhydrous THF (100 mL × 3) and anhydrous acetone (100 mL × 3), centrifuged and dried under vacuum at room temperature for 24 h, to obtain CuPc-MIDA-COF as a dark red powder with a yield of 91%. Elemental analysis: Calcd. C (65.92%), H (2.77%), N (8.54%). Found C (65.61%), H (3.03%), N (8.92%).

Instrumentation and Characterization

^{1}H NMR spectra were measured with a JEOL model JNM-LA400 NMR spectrometer. Fourier transform infrared (FT IR) spectra were recorded with a JASCO model FT/IR-6100 infrared spectrometer. Elemental analysis was performed with a Yanako CHN CORDER MT-6 elemental analyzer. Powder X-ray diffraction (PXRD) data were recorded with a Rigaku model RINT Ultima III diffractometer by placing the powder on a glass substrate. The angle 2ϑ was varied from 1.5° up to 40° with a 0.02° increment. A thermal gravimetric analysis (TGA) was performed with a METTLER TOLEDO model TGA/SDTA851[e].

Nitrogen Sorption Isotherm Measurements

Nitrogen sorption isotherms were measured at 77 K with a Micromeritics Instrument Corporation model 3Flex surface characterisation analyser. Before measurement, the samples were degassed in vacuum at room temperature for 24 h. The Brunauer-Emmett-Teller (BET) method was utilised to calculate the specific surface areas. By using the non-local density functional theory (NLDFT) model, the pore size distribution was derived from the adsorption curve.

Crystal Structure Simulations

The crystalline structure of HHTP-MIDA-COF and CuPc-MIDA-COF was determined using the density-functional tight-binding (DFTB+) method. The calculations were carried out with the DFTB+ program package version 19.1.[33, 34] DFTB utilises an optimised minimal LCAO Slater-type all-valence basis set in combination with a two-centre approximation for Hamiltonian matrix elements. The Coulomb interaction between partial atomic charges was determined using the self-consistent charge (SCC) formalism. Lennard-Jones type dispersion was employed in all calculations to describe van der Waals and π-stacking interactions.

For each COF, the monolayer, AA (eclipsed), AB (staggered) and slipped-AA structures were optimised using DFTB+ version 19.1. Where possible, DFTB parameters from the dftb.org website were employed as follows. Parameters for X–Y element pairs (X, Y = B, C, N, O and H) interactions were selected from the matsci-0-3 set and in the case of CuPc-MIDA-COF, Cu–X (X = C, H, O and N) parameters were taken from the slko.5425 set.

Following optimization of the geometry, the monolayer and lowest energy AA structures, the electronic band structures, and density of states were calculated at the DFT level using AMS-BAND (BAND 2019.3, SCM, Theoretical Chemistry, Vrije Universiteit, Amsterdam, The Netherlands, http://www.scm.com). Calculations used the PBE-D3 functional, DZ basis set with scalar relativity. Calculations were undertaken on both the DFTB output structures, which contained some deviation from symmetric unit cells (i.e., $a \approx b$, ⊠ ≈ 90° and symmetrised unit cells, $a = b$, ⊠ = 90°). To account for the Cu d-electrons, the DFT+U method was used. BAND has implemented a single parameter DFT+U method, the Coulomb (U) parameter of 4 eV was employed.

Molecular modelling and Pawley refinement were carried out using Reflex, a software package for crystal determination from XRD patterns. This was implemented in MS modelling version 8 (Accelrys Inc.). Initially, the unit cell dimensions were taken from the DFTB calculation and the space group for the crystal system was selected. We performed Pawley refinement to optimise the lattice parameters iteratively until the R_{WP} value converged. The pseudo–Voigt profile function was used for whole profile fitting and the Berrar–Baldinozzi function was used for asymmetry correction during the refinement processes.

To gain further insight into the in-plane and out-of-plane conduction in both HHTP-MIDA-COF and CuPc-MIDA-COF, one-dimensional wires, consisting of CuPc, HHTP nodes and MIDA linkers were cut from the lowest energy AA structures and capped with hydrogen atoms. The electronic band structures and density of states of these hydrogen-capped wires were then calculated using AMS-BAND as above.

Electronic Coupling and Reorganization Energy Calculations

To translate these rates into estimates for electron and hole mobility, we make the following simplifying assumptions. First, charge transfer within layers or diagonally across layers is assumed to be negligible, allowing us to focus on a single charge transfer pathway. This assumption simplifies the expression for charge carrier diffusion to equation (1).

$$D = \frac{d^2}{6} k_{CT} \quad \text{(eq. 1)}$$

Next, the interlayer distance d of COFs is taken directly from the corresponding PXRD crystal structure analysis. Finally, the charge carrier mobility is directly obtained from equation (2).

$$\mu = \frac{q}{k_B T} D \quad \text{(eq. 2)},$$

where q is the magnitude of the charge on the electron or hole undergoing transport.

The reorganization energy quantifies the energetic penalty associated with the distortion of COF linkers from their initial state that would be required to achieve the minimum-energy geometry for the final state without an actual transfer of charge. In this investigation, we adopt the four-point approximation to estimate the reorganization energy by the following equation (3).

$$\lambda_{\pm} = E(\pm|0) - E(\pm|\pm) + E(0|\pm) - E\big((0|0)\big) \quad \text{(eq. 3)}$$

These optimised geometries and energies[44] were obtained via Kohn-Sham density functional theory at the ωB97X-D/6-31G(d) level in Q-Chem 5.0.

Magneto-Transport Measurements

Device fabrication. The powders of CuPc-MDIA-COF and HHTP-MIDA-COF were mechanically pressed into homogeneous, round-shape pellets (with an average thickness of 0.4 mm and diameter of 7.0 mm) inside an argon-filled glove box under a pressure of 1.3 GPa. Then, the pellets were glued onto a gold-plated 24-pin sample holder using adhesive tape. The contacts in the Van der Pauw devices were made of metallic indium wires, which connected the pins to the outmost edges of the pellets (Figure. S9-10). Indium possesses many advantages compared to the commonly used silver contacts. It is a soft metal with a low electrical resistivity of 83.7 nΩ·m and has a low melting point (156.6 °C). The later allows for easy processing and moulding into the desired shape. Indium contacts usually adhere well to the sample surface. Hence, the use of additional silver paste can be avoided, which is beneficial also for the contact resistance.

Electronic property measurements. The conductivity and mobility of the compressed pellets were measured by using a Physical Property Measurement System (PPMS Dynacool, Quantum Design) across the temperature range from 240 to 300 K. Four terminal measurements were employed to exclude the contact effects (Figure. S9-10). All contacts in the van der Pauw configuration displayed a linear current-voltage characteristic, i.e. they were ohmic. This indicates that the Schottky barrier at the metal-semiconductor junction is small. Two characteristic resistances R_A and R_B were measured to calculate the pellet resistance (R_s) according to the Van der Pauw equations.[35]

$$\exp(-\pi R_A/R_s) + \exp(-\pi R_B/R_s) = 1 \quad \text{(eq. 4)}$$
$$R_A = R_{12, 43} = V_{43}/I_{12} \quad \text{(eq. 5)}$$
$$R_B = R_{14, 23} = V_{23}/I_{14} \quad \text{(eq. 6)}$$

In a typical experiment, a DC current was applied between contact 1 and 2 and the voltage across the opposite, the remaining contacts 3 and 4 were recorded to evaluate R_A (fig. 5). The same process was repeated to measure R_B.

The electrical conductivity σ (S cm^{-1}) of the pellets can be extracted using

$$\sigma = (R_s\, d)^{-1} \quad \text{(eq. 7)}$$

where d is the thickness (cm) of the pellets.

The Hall effect. Hall measurements were performed to determine the carrier density (n_s) and mobility (μ). The Hall voltage was measured between contacts 1 and 3 ($V_H = V_{13}$) in the presence of a perpendicular magnetic field of magnitude B by applying a current ($I = I_{24}$) between contacts 2 and 4 (Supplementary Fig. 9). The carrier density was calculated according to equation 8.

$$n_s = IB / (e\gamma V_H) \quad \text{(eq. 8)}$$

Here, e is the elementary charge (1.602×10^{-19} C) and γ is the Hall scattering factor. The γ value considers the energy dependence of the dominant scattering mechanism. It is smaller than 2 for all known scattering mechanisms and typically close to 1. Its calculation is a complex task requiring a specific model of the scattering mechanism. Therefore, it is commonly set equal to the typical value of 1. Electron and hole-like conduction can be distinguished by the polarity of the Hall voltage. Once the carrier density is known, the mobility follows equation 9.

$$\mu = |V_H| / (IBR_s) = 1 / (n_s e R_s) \quad \text{(eq. 9)}$$

Two-band model for the Hall effect. The non-linear behaviour of the Hall resistance in Figure 3F of the main text is characteristic for the co-existence of multiple charge carrier species. The simplest conceivable case to describe this behaviour is a two band or two channel model[46]

$$R_{xy} = \frac{B}{e} \cdot \frac{(\mu_1^2 n_1 + \mu_2^2 n_2) + (\mu_1 \mu_2 B)^2 (n_1 + n_2)}{(\mu_1 |n_1| + \mu_2 |n_2|)^2 + (\mu_1 \mu_2 B)^2 (n_1 + n_2)^2} \quad \text{(Eq. 10)}$$

Here, R_{xy} is the Hall resistance, B is the magnetic field and e is the elementary electron charge. n_1 and n_2 refer to the carrier densities of the two carrier types. The mobilities are denoted as μ_1 and μ_2.

At low magnetic field, i.e. $B \ll 1T$,

$$R_{xy} = \frac{B}{e} \cdot \frac{\mu_1^2 n_1 + \mu_2^2 n_2}{(\mu_1|n_1| + \mu_2|n_2|)^2} \quad \text{(Eq. 11)}$$

At high field, i.e. $B \gg 1T$,

$$R_{xy} = \frac{B}{e} \cdot \frac{1}{n_1 + n_2} \quad \text{(Eq. 12)}$$

At high field, the slope is positive and, hence,

$$\frac{1}{n_1 + n_2} > 0 \quad \text{(Eq. 13)}$$

$$(n_1 + n_2) > 0 \quad \text{(Eq. 14)}$$

This implies that the majority of the charge carriers are electrons. Either two electron ($2e^-$) pockets/channels or one electron (n_1) and one hole (n_2) pocket/channel co-exist with $n_1 > |n_2|$.

The difference in slope, Δ, between low field and high field is given by

$$\Delta = \frac{\mu_1^2 n_1 + \mu_2^2 n_2}{(\mu_1|n_1| + \mu_2|n_2|)^2} - \frac{1}{n_1 + n_2} = \frac{(\mu_1^2 n_1 + \mu_2^2 n_2)(n_1 + n_2) - (\mu_1|n_1| + \mu_2|n_2|)^2}{(\mu_1|n_1| + \mu_2|n_2|)^2 \, (n_1 + n_2)} \quad \text{(Eq. 15)}$$

The experimental data shows that $\Delta > 0$,

Since $(n_1 + n_2) > 0$ Eq. (14), the numerator in Eq. (15) must be larger than 0, therefore

$$(\mu_1^2 n_1 + \mu_2^2 n_2)(n_1 + n_2) > (\mu_1|n_1| + \mu_2|n_2|)^2$$
$$\rightarrow \mu_1^2 n_1^2 + \mu_2^2 n_1 n_2 + \mu_1^2 n_1 n_2 + \mu_2^2 n_2^2 > \mu_1^2 n_1^2 + 2\mu_1\mu_2|n_1 n_2| + \mu_2^2 n_2^2$$
$$\rightarrow (\mu_1^2 + \mu_2^2) n_1 n_2 > 2\mu_1\mu_2|n_1 n_2| > 0$$

It follows that both $n_1 > 0$ and $n_2 > 0$. The charge carriers in this sample are both electrons but they have different mobilities. We conclude that HHTP-MIDA-COF is an n-type semiconductor.

THz conductivity characterizations

THz conductivity measurements were carried out with an optical pump-THz probe (OPTP) scheme where a commercial, regenerative Ti: sapphire femtosecond amplifier system is employed to generate laser pulses with a central wavelength of 800 nm, a pulse duration of ~ 100 fs and a repetition rate of 1 kHz. A small fraction of the laser output was split and focused onto a 1 mm thick ZnTe (110) crystal. This allows the production of single-cycle THz probe pulses (~ 1 ps) covering frequencies from 0.4 to 2.0 THz through optical rectification. The generated THz pulses were then focused on the material of interest by a pair of off-axis parabolic mirrors. The transmitted divergent THz pulses were then collimated and focused by another pair of off-axis parabolic mirrors onto a second 1 mm thick ZnTe (110) crystal, where the transient THz electric field can be detected via electro-optic sampling. The detection principle is based on the fact that the transient THz electric field can modulate and is linearly proportional to the refractive index change of the second ZnTe crystal. By varying the time delay of the sampling beam and varying its time delay with respect to the THz pulse, one can readily map out the transmitted THz waveform in the time-domain.

To study the temporal evolution of the THz conductivity spectrum under nonequilibrium conditions following photoexcitation, HHTP-MIDA-COF or CuPc-MIDA-COF samples (both ~300 μm thick) were both sandwiched between two fused silica substrates and excited at 400 nm with a pump fluence of 252 μJ cm^{-2}. The 400 nm pump pulses were generated by frequency doubling 800 nm laser pulses using a BiB$_3$O$_6$ crystal.

The frequency-resolved complex photoconductivity of HHTP-MIDA-COF and CuPc-MIDA-COF were measured at 0.5 ps after the peak photoconductivity to avoid hot carrier effects. The data points were fitted to the Drude-Smith (DS) model using equation 16.

$$\sigma_{DS}(\omega) = \frac{\omega_p^2 \varepsilon_0 \tau}{1 - i\omega\tau} \times \left(1 + \frac{c}{1 - i\omega\tau}\right) \quad \text{(eq. 16)}$$

Here ω_p, ε_0 and τ represent plasma frequency, vacuum permittivity and scattering rate, respectively. We estimate charge mobilities of HHTP-MIDA-COF and CuPc-MIDA-COF samples in the DC limit ($\omega \rightarrow 0$) based on equation 16, which leads to equation 17.

$$\sigma_{DS}(\omega) = \omega_p^2 \varepsilon_0 \tau(1 + c) = eN\mu \quad \text{(eq. 17)}$$

where $\mu = \frac{e\tau}{M^*}(1 + c)$ and $N = \frac{\omega_p^2 \varepsilon_0 M^*}{e^2}$.

The curve fit using the Drude-Smith model yields a c parameter of -0.81 ± 0.04 for CuPc-MIDA-COF and -0.85 ± 0.06 for HHTP-MIDA-COF, respectively.

Resource Availability

Lead Contact

Further information and requests for resources should be directed to and will be fulfilled by the Lead Contact, Donglin Jiang (chmjd@nus.edu.sg).

Materials Availability
This study did not generate new unique reagents.

AUTHOR CONTRIBUTIONS
D.J. conceived the project, designed experiments, and provided funding. E.J. and K.G. conducted the experiments. M.A., N.K., N.K., H.X. and T.K. performed computational calculations. S.Y., J.G. and J.S. conducted Hall effect measurements. S.F., M.B. and H.W. carried out terahertz spectroscopy measurements. D.J., E.J. and K.G. wrote the manuscript and all authors commented on and revised the manuscript. E. Jin and K. Geng contributed equally.

DECLARATION OF INTERESTS
The authors declare no competing interests.

REFERENCES*
1. Günes, S., Neugebauer, H., and Sariciftci, N.S. (2007). Conjugated polymer-based organic solar cells. Chem. Rev. *107*, 1324–1338.

2. Kroon, R., Mengistie, D.A., Kiefer, D., Hynynen, J., Ryan, J.D., Yu, L., and Müller, C. (2016). Thermoelectric plastics: from design to synthesis, processing and structure–property relationships. Chem. Soc. Rev. *45*, 6147–6164.

3. Margolis, J. (2012). Conductive Polymers and Plastics. (Springer Science and Business Media).

4. Noriega, R., Rivnay, J., Vandewal, K., Koch, F.P., Stingelin, N., Smith, P., Toney, M.F., and Salleo, A. (2013). A general relationship between disorder, aggregation and charge transport in conjugated polymers. Nat. Mater. *12*, 1038–1044.

5. Klauk, H. (2012). Organic Electronics II: More Materials and Applications (Wiley-VCH).

6. Coropceanu, V., Cornil, J., da Silva Filho, D.A., Olivier, Y., Silbey, R., and Brédas, J.L. (2007). Charge transport in organic semiconductors. Chem. Rev. *107*, 926–952.

7. Cirera, B., Sánchez-Grande, A., de la Torre, B., Santos, J., Edalatmanesh, S., Rodríguez-Sánchez, E., Lauwaet, K., Mallada, B., Zbořil, R., Miranda, R., et al. (2020). Tailoring topological order and π-conjugation to engineer quasi-metallic polymers. Nat. Nanotechnol. *15*, 437–443.

8. Abbaszadeh, D., Kunz, A., Kotadiya, N.B., Mondal, A., Andrienko, D., Michels, J.J., Wetzelaer, G.J.A., and Blom, P.W. (2019). Electron trapping in conjugated polymers. Chem. Mater. *31*, 6380–6386.

9. Silins, E., and Capek, V. (1994). Organic Molecular Crystals: Interaction, Localization, and Transport Phenomena. (New York: AIP).

10. Poelking, C., and Andrienko, D. (2013). Effect of polymorphism, regioregularity and paracrystallinity on charge transport in poly (3-hexylthiophene)[P3HT] nanofibers. Macromolecules *46*, 8941–8956.

11. Huang, C.F., Wu, S.L., Huang, Y.F., Chen, Y.C., Chang, S.T., Wu, T.Y., Wu, K.Y., Chuang, W.T., and Wang, C.L. (2016). Packing principles for donor–acceptor oligomers from analysis of single crystals. Chem. Mater. *28*, 5175–5190.

12. Geng, K., He, T., Liu, R., Dalapati, S., Tan, K.T., Li, Z., Tao, S., Gong, Y., Jiang, Q., and Jiang, D. (2020). Covalent organic frameworks: design, synthesis, and functions. Chem. Rev. *120*, 8814–8933.

13. Jiang, D. (2020). Covalent organic frameworks: an amazing chemistry platform for designing polymers. Chem. *6*, 2461–2483

14. Xu, W., Tu, B., Liu, Q., Shu, Y., Liang, C. C., Diercks, C. S., Yaghi, O.M., Zhang, Y.-B., Deng, H. and Li, Q. (2020). Anisotropic reticular chemistry. Nat. Rev. Mater. *5*, 764-779.

15. Rodríguez-San-Miguel, D., Montoro, C., and Zamora, F. (2020). Covalent organic framework nanosheets: preparation, properties and applications. Chem. Soc. Rev. *49*, 2291–2302.

16. Han, X., Yuan, C., Hou, B., Liu, L., Li, H., Liu, Y. and Cui, Y. (2020). Chiral covalent organic frameworks: design, synthesis and property. Chem. Soc. Rev. *49*, 6248–6272.

17. Lohse, M. S. and Bein, T. (2018). Covalent organic frameworks: structures, synthesis, and applications. Adv. Funct. Mater. *28*, 1705553.

18. Wan, S., Guo, J., Kim, J., Ihee, H., and Jiang, D. (2008). A belt-shaped, blue luminescent and semiconducting covalent organic framework. Angew. Chem. Int. Ed. *47*, 8826–8830.

19. Jin, E., Asada, M., Xu, Q., Dalapati, S., Addicoat, M. A., Brady, M. A., Xu, H., Nakamura, T., Heine, T., Chen, Q., et al. (2017). Two-dimensional sp^2 carbon–conjugated covalent organic frameworks. Science *357*, 673–676.

20. Spitler, E. L., Colson, J. W., Uribe‐Romo, F. J., Woll, A. R., Giovino, M. R., Saldivar, A., and Dichtel, W. R. (2012). Lattice expansion of highly oriented 2D phthalocyanine covalent organic framework films. Angew. Chem. Int. Ed. *51*, 2623–2627.

21. Dalapati, S., Addicoat, M., Jin, S., Sakurai, T., Gao, J., Xu, H., Irle, S., Seki, S., and Jiang, D. (2015). Rational design of crystalline supermicroporous covalent organic frameworks with triangular topologies. Nat. Commun. *6*, 7786.

22. Kuhn, P., Antonietti, M., and Thomas, A. (2008). Porous, covalent triazine-based frameworks prepared by ionothermal synthesis. Angew. Chem. Int. Ed. *47*, 3450–3453.

23. Yue, Y., Cai, P., Xu, X., Li, H., Chen, H., Zhou, H.-C., and Huang, N. (2021). Conductive metallophthalocyanine framework films with high carrier mobility as efficient chemiresistors. Angew. Chem. Int. Ed. *19*, 10806-10813.

24. Wang, M., Wang, M., Lin, H.H., Ballabio, M., Zhong, H., Bonn, M., Zhou, S., Heine, T., Cánovas, E., Dong, R., et al. (2020). High-mobility semiconducting two-dimensional conjugated covalent organic frameworks with p-type doping. J. Am. Chem. Soc. *142*, 21622–21627.

25. Feng, X., Liu, L., Honsho, Y., Saeki, A., Seki, S., Irle, S., Dong, Y., Nagai, A., and Jiang, D. (2012). High-rate charge-carrier transport in porphyrin covalent organic frameworks: switching from hole to electron to ambipolar conduction. Angew. Chem. Int. Ed. *51*, 2618-2622.

26. Ding, X., Chen, L., Honsho, Y., Feng, X., Saengsawang, O., Guo, J., Saeki, A., Seki, S., Irle, S., Nagase, S., et al. (2011). An *n*-channel two-dimensional covalent organic framework. J. Am. Chem. Soc. *133*, 14510-14513.

27. Stalder, R., Mei, J., Graham, K.R., Estrada, L.A., and Reynolds, J.R. (2014). Isoindigo, a versatile electron-deficient unit for high-performance organic electronics. Chem. Mater. *26*, 664-678.

28. Wang, E., Mammo, W., and Andersson, M.R. (2014). 25th anniversary article: isoindigo-based polymers and small molecules for bulk heterojunction solar cells and field effect transistors. Adv. Mater. *26*, 1801-1826.

29. Lei, T., Wang, J.-Y., and Pei, J. (2014). Design, synthesis, and structure–property relationships of isoindigo-based conjugated polymers. Acc. Chem. Res. *47*, 1117-1126.

30. Gao, Y., Deng, Y., Tian, H., Zhang, J., Yan, D., Geng, Y., and Wang, F. (2017). Multifluorination toward high-mobility ambipolar and unipolar *n*-Type donor–acceptor conjugated polymers based on isoindigo. Ad. Mater. *29*, 1606217.

31. Cote, A.P., Benin, A.I., Ockwig, N.W., O'Keeffe, M., Matzger, A.J., and Yaghi, O.M. (2005). Porous, crystalline, covalent organic frameworks. Science *310*, 1166–1170.

32. Martínez-Abadía, M., Stoppiello, C.T., Strutynski, K., Lerma-Berlanga, B., Martí-Gastaldo, C., Saeki, A., Melle-Franco, M., Khlobystov, A.N., and Mateo-Alonso, A. (2019). A wavy two-dimensional covalent organic framework from core-twisted polycyclic aromatic hydrocarbons. J. Am. Chem. Soc. *141*, 14403–14410.

33. Aradi, B., Hourahine, B., and Frauenheim, T. (2007). DFTB+, a sparse matrix-based implementation of the DFTB method. J. Phys. Chem. A *111*, 5678–5684.

34. www.dftb.org

35. Van der Pauw, L.J. (1958). A method of measuring specific resistivity and Hall effect of discs of arbitrary shape. Philips Res. Repts. *13*, 1–9.

36. Shirakawa, H., Louis, E.J., MacDiarmid, A.G., Chiang, C.K., and Heeger, A.J. (1977). Synthesis of electrically conducting organic polymers: halogen derivatives of polyacetylene,(CH)$_x$. J. Chem. Soc., Chem. Commun. 578–580.

37. Rode, D.L. (1973). Theory of electron galvanomagnetics in crystals: Hall effect in semiconductors and semimetals. physica status solidi (b) *55*, 687–696.

38. Ulbricht, R., Hendry, E., Shan, J., Heinz, T.F., and Bonn, M. (2011). Carrier dynamics in semiconductors studied with time-resolved terahertz spectroscopy. Rev. Mod. Phys. *83*, 543–586.

39. Wang, M., Ballabio, M., Wang, M., Lin, H.H., Biswal, B.P., Han, X., Paasch, S., Brunner, E., Liu, P., Chen, M., et al. (2019). Unveiling electronic properties in metal–phthalocyanine-based pyrazine-linked conjugated two-dimensional covalent organic frameworks. J. Am. Chem. Soc. *141*, 16810–16816.

40. Cocker, T.L., Baillie, D., Buruma, M., Titova, L.V., Sydora, R.D., Marsiglio, F., and Hegmann, F.A. (2017). Microscopic origin of the Drude-Smith model. Phys. Rev B *96*, 205439.

41. Berlin, Y.A., Hutchison, G.R., Rempala, P., Ratner, M.A., and Michel, J. (2003). Charge hopping in molecular wires as a sequence of electron-transfer reactions. J. Phys. Chem. A *107*, 3970–3980.

42. Kitoh-Nishioka, H., Welke, K., Nishimoto, Y., Fedorov, D.G., and Irle, S. (2017). Multiscale simulations on charge transport in

covalent organic frameworks including dynamics of transfer integrals from the FMO-DFTB/LCMO approach. J. Phys. Chem. C *121*, 17712–17726.

43. Wu, Q., Kaduk, B., and Voorhis, T.V. (2009). Constrained density functional theory-based configuration interaction improves the prediction of reaction barrier heights. J. Chem. Phys. *130*, 034109.

44. Shao, Y., Gan, Z., Epifanovsky, E., Gilbert, A.T., Wormit, M., Kussmann, J., Lange, A.W., Behn, A., Deng, J., Feng, X., et al. (2015). Advances in molecular quantum chemistry contained in the Q-Chem 4 program package. Mol. Phys. *113*, 184–215.

45. Patwardhan, S., Kocherzhenko, A. A., Grozema, F. C., and Siebbeles, L. D. (2011). Delocalization and mobility of charge carriers in covalent organic frameworks. J. Phys. Chem. C *115*, 11768–11772.

46. Mashhadi, S., Kim, Y., Kim, J., Weber, D., Taniguchi, T., Watanabe, K., Park, N., Lotsch, B., Smet, J.H., Burghard, M., et al. (2019). Spin-split band hybridization in graphene proximitized with α-RuCl$_3$ nanosheets. Nano Lett., *19*, 4659-4665.